

A numerical model for steady-state temperature distributions in solid-medium high-pressure cell assemblies

JOHN HERNLUND,^{1,2} KURT LEINENWEBER,^{3,*} DARREN LOCKE,^{1,4} AND JAMES A. TYBURCZY¹

¹Department of Geological Sciences, Arizona State University, Tempe, Arizona 85287-1404, U.S.A.

²Current address: Department of Earth and Space Sciences, University of California, Los Angeles, Los Angeles, California 90095-1567, U.S.A.

³Department of Chemistry and Biochemistry, Arizona State University, Tempe, Arizona 85287-1404, U.S.A.

⁴Current Address: Mineral Physics Institute, Stony Brook University, Earth and Space Sciences Building 255, Stony Brook, New York 11794-2100, U.S.A.

ABSTRACT

We present a numerical model for calculating the temperature distribution inside resistance-heated high-pressure solid-medium axi-symmetric cell assemblies that incorporates both composition- and temperature-dependent thermal conductivity. The code was validated using both analytic solutions of simplified thermal diffusion problems and comparisons to actual laboratory experiments and was found to be reliable in matching the temperature characteristics of multi-anvil experiments. Calculations for various cell assembly designs resulted in temperature fields that are consistent with experimental measurements of thermal gradients. These calculations also illustrated the influence of temperature-dependence of thermal conductivity, an important and often-overlooked property, on the thermal profiles. This model may be used to fine-tune the design of cell assemblies, either to minimize thermal gradients or to produce a desired temperature distribution. The four “typical” multi-anvil cells that we used to demonstrate this technique have temperature profiles across the sample that range from 25 to 75 °C when the thermocouple temperature is 1200 °C. The thermocouple in all four is in a region where the temperature gradient is on the order of 100 °C per millimeter, which could lead to experimental temperature uncertainties that are correlated with the thermocouple location.

Keywords: Multi-anvil, high pressure, thermal gradients, temperature, numerical modeling

INTRODUCTION

Solid-medium high-pressure devices are in widespread use for the replication of conditions that exist in the Earth’s interior, or for the synthesis and study of materials at high pressures and temperatures. The typical solid-medium device consists of a ram that exerts a force on an arrangement of anvils, which in turn exert forces on a solid but ductile container for the sample. An electrically heated resistance furnace may be placed inside the container, with a thermocouple and a sample. Due to practical fabrication considerations, the geometry of the innermost parts of the sample assembly is often (but not always) cylindrical, or can be closely approximated as cylindrical.

The primary advantages of solid-medium high-pressure techniques include a relatively large sample volume, stable temperature control, and the ability to perform long duration experiments. Further advantage could be obtained by controlling the temperature distribution using carefully designed assemblies. Uncontrolled thermal gradients, on the other hand, not only decrease the temperature resolution of experiments, but may also lead to anomalous effects in the chemistry of the sample (Schmidt and Ulmer 2004).

Thermal gradients in solid samples are the result of heat transport by conduction. Because it is seated inside a cylindrical furnace, the temperature inside a sample tends to increase

radially from its center. Also, the furnace has a finite axial extent, inducing heat conduction along the assembly axis and causing cooler temperatures to prevail away from the center of a sample in the axial direction. Thus a simple assembly consisting of a uniform thickness furnace and solid-medium materials produces roughly paraboloid isotherms (opening in the axial direction away from the sample center) with temperature variations sometimes exceeding 100 °C across the sample. This gives rise to the hourglass-shaped compositional or phase layering frequently observed in high-pressure samples. The problem is exacerbated when the furnaces are short relative to their radii, decreasing the axial extent and enhancing axial conduction. Examples of high-pressure experiments where this is the case are multi-anvil experiments (Kawai and Endo 1970; Walker et al. 1990) with assembly sizes on the order of a few millimeters, and experiments using opposed-anvil presses such as the Bridgman device (cf. Ringwood and Major 1966) and the Drickamer cell (Funamori and Yagi 1993; Yamazaki and Karato 2001).

Several types of measurements can be made to estimate or calibrate the thermal gradients in high-pressure experiments. One such calibration would be measurement of a standard temperature relative to the temperature of the thermocouple; for example, determination of the melting front in a single component metal (e.g., gold) as a function of the temperature at a nearby thermocouple (Bertka, pers. comm.). Or, more than one thermocouple may be placed in selected locations in the

* E-mail: kurtl@asu.edu

assembly, and the temperatures compared; due to experimental limitations, two thermocouples are normally used, providing two discrete points in the thermal profile (cf. Gwanmesia et al. 1990). A multi-phase sample with a calibrated, temperature-dependent reaction between some of the phases, such as the two-pyroxene geothermometer (e.g., Walter et al. 1995; Bertka and Fei 1997), could also be used to study the thermal gradient. Recently, van Westrenen et al. (2003) used variations in the thickness of the reaction front between MgO and Al₂O₃ as a sensitive and detailed measure of the temperature gradient (Watson et al. 2002). All of these experimental techniques provide information about thermal gradients in actual experiments. Finally, the hourglass-shaped phase or chemical segregation in many experimental samples, although not usually giving the magnitude of the temperature gradient, often reveal the shapes of the isotherms.

In addition to these experimental methods, it would be very useful to obtain reliable a priori quantitative estimates of thermal gradients in solid-medium assemblies from the geometry combined with the heat output of the furnace and the thermal conductivities of the samples and other materials. This could be used for many purposes, such as refinement or extension of experimentally measured thermal gradients to a larger region in space, collection of information about thermal gradients that have not yet been directly measured, and guidance in the design of new assemblies having well-regulated internal temperature distributions. Another reason to desire good thermal models is that the thermal gradient can be sample- and capsule-dependent, which requires a means of transforming the gradients measured in one configuration into gradients relevant to each experiment. Also, a well-controlled temperature distribution might eventually allow accurate measurement of both the thermal diffusivity in time-dependent heating experiments (e.g., Katsura 1997) and the thermal conductivity of a sample. In practical terms, the expense involved in materials and time spent preparing and analyzing adequate experimental temperature calibrations can be substantially reduced when replaced or supplemented by a realistic numerical model.

In this paper, we present a numerical model for calculating thermal profiles in solid-medium high-pressure cell assemblies. The model begins with the assumption of axi-symmetric geometry. The outer boundaries of the cylinder are constrained to be either uniform temperature or insulating (i.e., zero-heat flux). The model allows for temperature-dependent thermal conductivities of the materials used in the cell assembly, including the sample. Heat sources may be placed anywhere within the assembly to represent the heat output of the furnace. The model itself is based on a flux-conservative numerical approximation that will be described in detail in the sections that follow. The model was used to calculate several standard types of furnace design in current use and to compare their features, and we found that the known aspects of their thermal gradients were reproduced to a good level of accuracy.

Another recent numerical investigation of temperature distributions has been applied to solid medium experiments in the piston-cylinder apparatus (Schilling and Wunder 2004), illustrating the usefulness of such models in designing and understanding experiments. Our model differs in many respects from this and other previous ones. Because our model describes steady-state

cases, no information regarding density or heat capacity is necessary. Our model also uses an approximate analytical expression to account for temperature variations inside the anvils, and therefore includes, in a simplified way, the entire press. We implemented an efficient multigrid solver in our code that can return steady solutions in a small amount of computational time, and allows for the use of dense grids for accurate modeling of small physical details. Finally, the model we present here has been thoroughly validated against analytical solutions for several scenarios, and we have included a graphical user interface with the code, to facilitate its use by the high-pressure experimental community (the program is deposited with this paper).

MODEL DESCRIPTION

Governing equations

In many practical applications, thermal diffusion is a simple linear problem where modest variations in temperature allow the modeler to assume that the thermal conductivity of the medium is constant. However, in environments exhibiting extreme temperature variations, such as heated solid-medium high-pressure assemblies, the corresponding variations in thermal conductivity are often significant. In this case, the heat equation is given by:

$$\rho c_p \dot{T} = \vec{\nabla} \cdot (K \vec{\nabla} T) + Q \quad (1)$$

where ρ is the density of the medium, c_p is its specific heat, T is the temperature, K is the thermal conductivity, Q is the heat production per unit volume, $\vec{\nabla}$ is the gradient vector, and an over-dot signifies a derivative with respect to time t . Equation 1 is non-linear, because K is a function of the dependent variable T .

Applying the condition of axi-symmetry, with radial coordinate r and axial coordinate z , in the time limit of steady-state, Equation 1 assumes the form:

$$\frac{1}{r} \frac{\partial}{\partial r} \left(r K \frac{\partial T}{\partial r} \right) + \frac{\partial}{\partial z} \left(K \frac{\partial T}{\partial z} \right) + Q = 0. \quad (2)$$

Note that the steady-state temperature distribution does not depend on the thermal inertia, ρc_p , and therefore information regarding density and specific heat is not necessary. Our assumption of axi-symmetry for octahedral assemblies leads to a negligibly small error in the temperature estimates near the center of the assembly. On the basis of a spherical harmonic analysis, one can show that this error propagates into the sample region with terms such as \bar{r}^l , where \bar{r} is the absolute distance from the center of the sample and l is the harmonic degree. For a linear octahedral perturbation to an axi-symmetric solution, the leading order terms will have $l \geq 4$, and thus decrease rapidly from the outer assembly into the sample region; the perturbations cancel at the center of the octahedron. For example, using a 14/8 mm octahedron with a sample 3 mm in diameter, we estimate that the octahedral perturbation at the sample edge will be reduced to less than 2% of the perturbation at the anvil faces. The same result is also obtained for assemblies having a cubic pressure medium. We thus conclude that the assumption of axi-symmetry is reasonable for thermal modeling of the sample volume in multi-anvil assemblies to a first order.

Numerical model

The numerical model was constructed over a domain of discrete rectangular cells using a flux-conservative formulation (cf. Oran and Boris 1987). The heat flux was defined at the center of cell faces and the temperature was defined at the cell centers, while the composition and heat production of each cell was taken to be uniform over its entire area. If we discretize the domain using $r_i = (i + 1/2)\Delta r$ and $z_j = (j + 1/2)\Delta z$ as the cell-center coordinates, where Δr and Δz are the radial and axial cell dimensions respectively (see Fig. 1), $i = 0, 1, \dots, N_r - 2, N_r - 1$, and $j = 0, 1, \dots, N_z - 2, N_z - 1$, the second-order flux-conservative approximation to Equation 2 is:

$$0 = \frac{1}{r_i(\Delta r)^2} (r_{i+1/2} K_{i+1/2,j} (T_{i+1,j} - T_{i,j}) + r_{i-1/2} K_{i-1/2,j} (T_{i-1,j} - T_{i,j})) + \frac{1}{(\Delta z)^2} (K_{i,j+1/2} (T_{i,j+1} - T_{i,j}) + K_{i,j-1/2} (T_{i,j-1} - T_{i,j})) + Q_{i,j} \quad (3)$$

where we have used subscripts to represent the value of a function at a given discrete coordinate position, e.g., for the temperature $T(r_i, z_j) = T_{i,j}$. The numerical formulation given by Equation 3 is a local expression for the conservation of energy in each cell (i.e., heat in equals heat out).

This particular discretization requires values for the thermal conductivity at cell faces, while thermal conductivity is naturally defined at cell centers. For these cell-face values, we used the so-called "harmonic interpolant" for the conductivity, which was constructed in such a way that it preserves the continuity of heat flux between adjacent cells and therefore exhibits a close correspondence to the physical process. The required conductivity

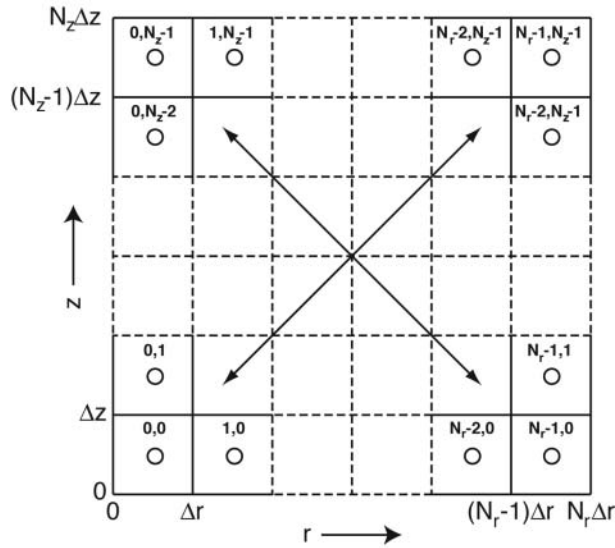


FIGURE 1. Layout of the computational grid showing the control volumes (or cells) and the cell-center locations where temperature and heat production are defined (circles). The heat flux and thermal conductivity were defined at the cell edges. The total number of cells along r is N_r , and along z is N_z , and each of these quantities was restricted to powers of 2. Also, in all of our calculations, only square grid elements were used, so that $\Delta r = \Delta z$. The bold face type in the cells indicate the values for i and j , while the radial and axial distances from the origin are indicated along the edges. The arrows indicate that many rows and columns of cells between the four corners are omitted from the diagram.

values in Equation 3 are given by:

$$K_{i+1/2,j} = 2K_{i,j}K_{i+1,j} / (K_{i,j} + K_{i+1,j}), \quad (4a)$$

$$K_{i,j+1/2} = 2K_{i,j}K_{i,j+1} / (K_{i,j} + K_{i,j+1}). \quad (4b)$$

Closure of the system of equations generated by Equation 3 requires suitably chosen boundary conditions at the edges of the domain. These boundary conditions are enforced by introducing rows of "ghost cells" just outside the domain (for $i = -1$, $i = N_r$, $j = -1$, and $j = N_z$) having the same dimensions as the adjacent interior cells. For a fixed temperature boundary condition, the ghost cells are assigned values such that the linear interpolant between the ghost cell temperature and the adjacent interior cell temperature yield the desired value. For a zero heat-flux boundary condition, the temperatures inside the ghost cells are assigned the same temperature as that in the adjacent interior cell. Because both of these boundary conditions are second-order, they preserve the overall second-order accuracy of the system generated by Equation 3. In addition, second-order accurate estimates of heat flux across fixed temperature boundaries are also made possible by this discretization. In all cases, the values of thermal conductivity in ghost cells are equivalent to those in the adjacent interior cells.

A critical aspect is the accurate reproduction of heat generation due to Ohmic dissipation in the furnace, as furnace design figures prominently in the achievement of controlled thermal gradients. For a furnace having a total electrical resistance R across the entire assembly, an electric current I passing through it produces a total power of $P = I^2 R = VI$, where V is the applied electric potential. Assuming zero loss through the rest of the circuit, all of this energy is dissipated as heat in the furnace, so that values determined from the power supply should give a good estimate of the total heat input in the assembly. In this model, the furnace is divided into discrete slabs that are in series, one slab per grid layer in the model. The relative heat production of each slab of cells within the furnace is set to be inversely proportional to the cross-sectional area it presents to the in-series current flow. This ensures that thin furnace parts produce a greater amount of heat than thick parts, e.g., in a stepped-furnace configuration, and also allows for either axial flow or radial flow in each furnace component, so that combination designs such as telescoping or box furnaces may be modeled. The heat sources are thus, for a given total current I :

$$Q_{i,j} = (I / A_{i,j})^2 \rho_{i,j} \quad (5)$$

where $\rho_{i,j}$ is the resistivity at the point (i,j) , and $A_{i,j}$ is the cross-sectional area of the furnace at the point (i,j) and perpendicular to the current flow; i.e., $2\pi r_i h$ for a radially directed furnace element of height h , or $\pi(r_{\text{outer}}^2 - r_{\text{inner}}^2)$ for an axially directed furnace element with outer radius r_{outer} and inner radius r_{inner} . In cases where furnace parts are not carrying significant amounts of current, such as the graphite pickup cap in the Watson assembly (see below), the furnace part is not assigned any heat output and simply behaves as any other passive or non-heating assembly part. The total power is obtained by taking the volume integral of Q over the grid, taken as a sum over the cells, and also multi-

plying by a symmetry factor s which is 1 if the entire furnace is modeled, and 2 if only half the furnace is modeled:

$$P = 2\pi s \sum_{i,j} Q_{ij} r_{i+1/2} \Delta r \Delta z. \quad (6)$$

In cases where resistivity is constant, this power can be compared to the theoretical power for the circuit, and was found to converge to the theoretical power as the grid density increases, as expected.

We ignore for the time being any segregation of the current into *parallel* shells due to temperature variation of conductivity in the direction perpendicular to the current flow, meaning that a “heat pipe” effect such as that hypothesized by Walker (pers. comm.) for thick lanthanum chromite furnaces is not considered. This effect may be tested in future versions of the model.

Boundary conditions

The model has four boundaries, defined by (1) $r = 0$, (2) $r = r_{\max} = N_r \Delta r$, (3) $z = 0$, and (4) $z = z_{\max} = N_z \Delta z$. The boundary conditions for the model were chosen to most closely match the situation encountered in a solid-medium apparatus while maintaining numerical simplicity and avoiding the necessity of introducing more parameters into the model. First, there are some necessary physical constraints on the boundaries. One constraint is that the boundary corresponding to $r = 0$ (i.e., the cylindrical axis of the model) is a zero horizontal-flux boundary because it lies on an axis of symmetry. A second constraint is that part or all of the remaining boundaries in the model act as heat sinks. In our model a heat sink is a segment or segments of the boundary that are held at a selected temperature.

When a cell assembly has mirror symmetry perpendicular to the cylindrical axis, the numerical problem may be simplified by choosing the $z = 0$ plane as a zero-flux boundary; this plane then coincides with the mirror plane in the cell assembly, and only one quadrant of the assembly cross-section has to be explicitly modeled. If the assembly is not mirror-symmetric, then the whole length of the assembly can be modeled by setting both the $z = 0$ plane and the $z = z_{\max}$ plane as isothermal boundaries.

It is simplest, and involves the fewest ad hoc assumptions, to impose the condition that all portions of the boundary that act as a heat sink are at a uniform temperature T_1 . This assumption is justified when the anvils have a significantly higher thermal conductivity than the pressure medium and when the boundary is sufficiently far from the sample. This boundary can be placed several millimeters into the anvils and this does not significantly affect the thermal gradient in the sample, an assertion that is easily tested by moving the boundary and recalculating the thermal gradient. However, the total power requirement was found to be significantly affected by this boundary position. Also, the temperature at this boundary is considerably higher than the ambient temperature (the anvils become hot during experiments), so the choice of the proper temperature for this boundary is a significant issue.

To account for this in the least arbitrary fashion, we introduced a model for the effect of the press on the thermal profile. In this model, we assumed that the press conducts heat away from the assembly toward some external heat bath maintained at a cooler temperature T_2 (e.g., cold water circulated through the outer

portions of the press, or air at room temperature), which is at a distance of hundreds of millimeters. We modeled the press as a large spherical-shell steel container with an effective radius r_2 on the order of hundreds of mm, surrounding an assembly with effective radius r_1 on the order of 10 mm. The volume of the model (including the mirror image part if an axial boundary is a mirror plane) was used to set r_1 according to $V = (4/3)\pi r_1^3$. The power from the furnace was modeled as a uniformly emitting source within the inner boundary at r_1 , i.e., the furnace was assumed to behave like a point source at $r = 0$ on the scale of the press. This geometry has an explicit solution (Carslaw and Jaeger, 1959):

$$T_1 = T_2 + [P / (4\pi K)](1/r_1 - 1/r_2) \quad (7)$$

In this formula, P is the total furnace power, T_1 is the temperature of the inner boundary of the press in contact with the high-pressure cell (which will be matched to the outer boundary of the finite-difference model), T_2 is the temperature of the water or air bath outside the press, and K is the thermal conductivity of the press. Because $r_2 \gg r_1$, this parameterization is not sensitive to the choice of r_2 . It is worthwhile to note that Equation 7 is a linear function of the source power, a result that is independent of the assumption of an effective spherical geometry for the press, e.g., one finds a similar relation for a cylindrical or square press, with a different geometrical constant. In the experiments presented here, we used a press radius r_2 of 114 mm, which was based on the distance from the sample to the isothermal boundary of a Walker module with a water-cooling jacket.

The model also includes the choice of having the temperature at the isothermal boundaries of the numerical grid fixed to a constant value, which is useful in instances where the temperature at the boundaries is known.

SOLUTION METHOD

The discretized equations were improved from an initial guess by employing a multigrid technique that utilizes a red-black Gauss-Seidel smoother at each grid level (Brandt 1977). By using a multigrid scheme, the amount of computational work required to achieve convergence is proportional to the number of grid points, whereas the work required in time integration (i.e., Jacobi-type) or Gauss-Seidel relaxations on the finest grid only is proportional to the square of the number of grid points. This increase in efficiency allows for the use of finer grids, permitting a detailed analysis of the thermal profiles and the effects of thin components such as metal foils. The best convergence was achieved when the model cells had a unit aspect ratio, thus we take $\Delta r = \Delta z$. Also, a multi-grid requires coarsening of the computational domain, so that N_r and N_z must be chosen as a power of two (i.e., 2, 4, 8, 16, 32, ...). This means in practical terms that the model is restricted to having a unit aspect ratio or an aspect ratio that is a power of two.

To test convergence, two methods were used. The first method used a global integration over the residual error in Equation 3, which measures the degree of local conservation of energy. If $N (= N_r N_z)$ is the total number of points inside the domain, the root-mean-square of the residual error is defined by:

$$\sqrt{\frac{1}{N} \sum_{i,j} res_{i,j}^2} \quad (8)$$

where summation over i,j excludes ghost cells and $res_{i,j}$ is the local residual of the governing equation, equal to the right-hand side of Equation 3. When both the temperature and conductivity values satisfy Equation 3, the residual must be zero. In practice, computers can never achieve a zero residual due to round-off and other sources of intrinsic errors, so the convergence criterion was chosen to make the root-mean-square of the residual error smaller than the truncation error of the scheme itself. Secondly, the sum of the total heat flux out of the constant-temperature boundaries of the model should converge to a value that is equivalent to the sum of all the heat sources in the model. This is given by

$$\sum_{i,j \in S} \bar{F}_{i,j} \cdot \hat{n} + \sum_{i,j} r_i Q_{i,j} = 0 \quad (9)$$

where the first sum on the left-side is taken over the boundaries, and $\bar{F}_{i,j} \cdot \hat{n} = K_{i,j}(T_{\text{ghost}} - T_{\text{in}})/(\Delta r, \Delta z)$ is the heat flux normal to the boundary where T_{ghost} is the ghost cell temperature and T_{in} is the adjacent interior cell temperature. This second criterion is a measure of the global conservation of energy, which is satisfied when the flux-conservative formulation is used.

PHYSICAL PROPERTIES OF CELL COMPONENTS

As has been mentioned, the physical properties needed to calculate thermal gradients in multi-anvil cells are the thermal conductivities and the electrical conductivities of the relevant materials. The accuracy of the model is probably most sensitive to these material properties, which vary widely from material to material and may be dependent on details such as phase changes, chemical doping, and pressure as well as temperature. Because so little information is available about these effects, we have mainly surveyed the data available for the temperature-dependent thermal conductivities at atmospheric pressure, while the electrical conductivities have been largely derived from the total furnace conductivity observed in our high-pressure experiments. The pressure effect is thought to be much smaller than effects of temperature in sufficiently stiff materials without phase transitions (e.g., Hofmeister 1999).

The thermal conductivity coefficients used in the calculations are shown in Table 1, and the variations with temperature are shown in Figures 2a and b. We restricted the analysis to polynomial fits that reproduce the data points but are not reliable for extrapolation. Models suitable for extrapolation will be desirable in the future for reliable results at very high temperatures.

Figure 2 shows that the thermal conductivity variations with temperature are very pronounced for some materials, and less so for others. This has effects on the relative contrast between materials; for example, the common idea that MgO is an excellent heat conductor compared to ZrO₂ becomes less true at high temperatures. Thus the efficacy of MgO as a heat distributor when placed inside zirconia is not as good as might be expected. This will be evident in some of the thermal gradients that are derived from the model.

For the electrical resistivity of graphite and lanthanum chromite, we used an Arrhenius temperature dependence of the form:

$$\rho = \rho_0 e^{-A/RT} \quad (10)$$

The coefficients for graphite ($\rho_0 = 8.85 \cdot 10^{-6} \Omega \cdot \text{m}$, $A = 2.35$ kJ/mole) were taken directly from Schilling and Wunder (2004), both for consistency with that study, and because these numbers give reasonable agreement with the overall resistance and the temperature dependence of resistance observed in our multi-anvil experiments using graphite furnaces. For the lanthanum chro-

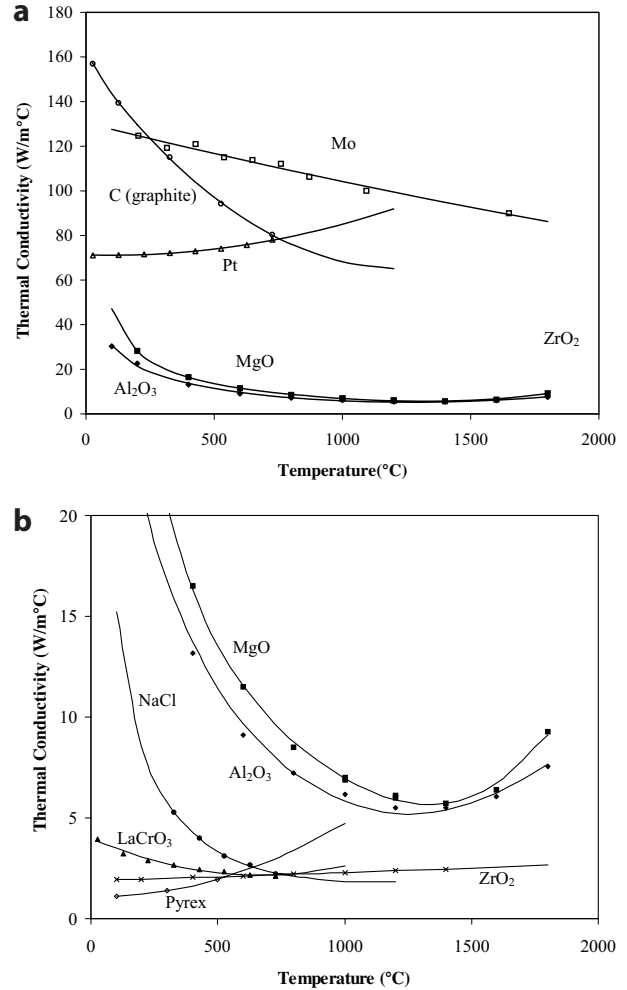


FIGURE 2. Thermal conductivities of materials modeled in this study, showing data points that were used in the fitting, and the fitted curves. (a) Focusing on the materials with higher thermal conductivities. (b) Focusing on the materials with lower thermal conductivities.

TABLE 1. Thermal conductivity coefficients used in this study, and references

| Material | $k = a + bT + cT^2 + dT^3 + gT^{-0.5}$ (W/m · °C) | | | | | Data T range (°C)* | Reference |
|--------------------------------|---|------------|------------|-----------|-----------|-----------------------|---------------------------------|
| | a | b | c | d | g | | |
| MgO | -2.523E+01 | 2.356E-02 | -2.108E-05 | 7.493E-09 | 7.012E+02 | 100-1200 | Kingery et al. (1954) |
| Mo | 1.303E+02 | -2.820E-02 | 2.064E-06 | | | 1000-1800 | McQuarrie (1954) |
| LaCrO ₃ | 3.979E+00 | -5.368E-03 | 3.979E-06 | | | 230-2225 | Hampel (1961) |
| Al ₂ O ₃ | 4.799E+00 | -1.461E-02 | 7.016E-06 | | 2.726E+02 | 30-725 | Sakai and Stolen (1995) |
| Pyrex-7740 | 1.052E+00 | -9.439E-17 | 3.663E-06 | | | 100-1800 | Kingery et al. (1954) |
| Pt | 7.126E+01 | -3.486E-03 | 1.726E-05 | | | 100-500 | Kingery (1959) |
| C (graphite) | 1.546E+02 | -1.482E-01 | 6.065E-05 | | 3.241E+01 | 30-725 | Laubitz and Van Der Meer (1966) |
| NaCl (2.9GPa) | -8.964E+00 | 3.278E-03 | | | 2.384E+02 | 30-725 | Taylor et al. (1968) |
| ZrO ₂ | 1.904E+00 | 3.307E-04 | 4.645E-08 | | | 330-725 | Fujisawa et al. (1968) |
| WC | 6.300E+01 | | | | | 100-1400 | Kingery et al. (1954) |
| Steel | 5.000E+01 | | | | | 25 | (typical value for WC) |
| | | | | | | 25 | (typical value for 4340 steel) |

* This column gives the range of temperature where measurements were made for each material.

mite resistivity, we derived values ($\rho_0 = 4.16 \cdot 10^{-4} \Omega \cdot \text{m}$, $A = 8.91$ kJ/mole) that are consistent with the resistances we measured in experiments with a straight LaCrO_3 heater in a 14/8 assembly. It should be noted that the pre-exponential factor ρ_0 has no effect on the temperature gradient, only on the overall resistance of the heater; however, the quantity A in the exponent has a significant effect on the temperature gradient. For platinum, we assumed a constant resistivity of $1.035 \cdot 10^{-7} \Omega \cdot \text{m}$.

Validation of the numerical approximation

To verify the numerical model, we tested it against exact solutions, which are available in special cases. For example, when a uniform, planar heat source was placed halfway along z , and the boundary temperatures at $r = 0$ and $r = r_{\text{max}}$ are set to a temperature T_1 while the boundary at $z = z_{\text{max}}$ was a zero-flux boundary, the temperature distribution within a uniform layer of material was linear, as expected. One way to test for the behavior in the r -direction is to compare the calculated temperature to the temperature distribution due to a linear heat source inside a composite circular cylinder, consisting of an arbitrary number of layers of material with differing thermal conductivities that are independent of temperature. This problem has the closed-form solution (Carslaw and Jaeger 1959, p. 190):

$$T = T_0 + \frac{Q \ln(r_0 / r)}{2\pi K} \quad (11)$$

where T is the temperature at any point within a cylindrical shell, T_0 is the temperature at the outer boundary of the shell, Q is the heat flow through the inner boundary of the shell per unit length, and K is the thermal conductivity of the shell, assumed to be independent of temperature. In the numerical model, the infinite cylinder is obtained by defining the boundaries at $z = 0$ and $z = z_{\text{max}}$ to be zero-flux boundaries, and the boundary at $r = r_{\text{max}}$ to be an isothermal boundary.

The solutions are compared in Figure 3, for composite cylinders composed of MgO (a relatively good thermal conductor) and ZrO_2 (a good thermal insulator) with their room-temperature conductivity values. We used a thermal conductivity for MgO of $55.2 \text{ W/m}\cdot\text{K}$ (Hofmeister, 1999) and for ZrO_2 of $1.91 \text{ W/m}\cdot\text{K}$. In these tests, we adjusted the electric current through the graphite rod until the surface of the rod reached a temperature of $1000 \pm 0.1 \text{ }^\circ\text{C}$. This was done because it resembles the calculation methods presented here for multi-anvil assemblies, where the electric current is adjusted until the thermocouple temperature reaches a desired value. The first reasonable approximation to the analytical solution was obtained for a grid size of 64×64 , where the RMS temperature error was 0.4% of the graphite surface temperature. A closer match was obtained for a grid size of 128×128 , where the rms error in temperature was 0.1% of the graphite surface temperature. Convergence in electric current and furnace power were around 1 to 2 percent. These results will vary with the individual geometries used. It should also be noted that the temperatures in Table 2a are based on linear interpolation between the grid points, and this also introduces an error, especially when the point is on a kink in the thermal profile. Thus, the best measure of the fidelity of a given model is the rms error, and the model can be considered most valid at the grid points themselves.

Alternatively, the power may be held constant at the analytical value for $1000 \text{ }^\circ\text{C}$, while the temperature field is solved. The results of such an approach are shown in Table 2b. In this case, the temperature accuracy is about four times worse. Fixing the temperature at one “known” point (such as the thermocouple) and letting the power change leads to a more accurate temperature profile for the types of problem of interest here.

This test problem also demonstrates the importance of the harmonic interpolation described above for sharp boundaries in thermal conductivity. When simple linear interpolations of conductivity are used at material boundaries, the system still converges toward the expected values as the number of cells is increased, but the convergence is much slower. In general, the temperatures nearer the center are underestimated when harmonic interpolation is not used, or equivalently the power is overestimated for a fixed internal temperature. The discrepancies occur at internal material boundaries, and the eventual convergence is due to the importance of the boundaries diminishing as the number of points increases. In light of this result, we adopted the harmonic interpolation scheme in all of the calculations presented here.

The effect of boundary distance and boundary condition was tested using four calculations on one real cell assembly. The “G2” multi-anvil cell assembly (Gwanmesia et al. 1990, also described in the results section) was used for these tests. Two boundary conditions, one at constant temperature ($25 \text{ }^\circ\text{C}$) and one modeling the press environment as an insulating container, were used; in both cases the boundary of the numerical grid was moved from 6 mm to 12 mm distance from the center point, to measure the effect on the temperature distribution. The press container was assumed to be made of steel with a thermal conductivity of $50 \text{ W/m}\cdot\text{K}$.

As may be seen in Table 3, modeling the press environment reduced the effect of moving the boundary on the thermal field in the sample by a factor of nearly five. The effect of moving the boundary on the calculated power required to reach $1200 \text{ }^\circ\text{C}$ was also reduced, by a factor of two. Including the press environment thus had the effect of “softening” the boundary effect on the quantities of interest. Because the real press environment (i.e.,

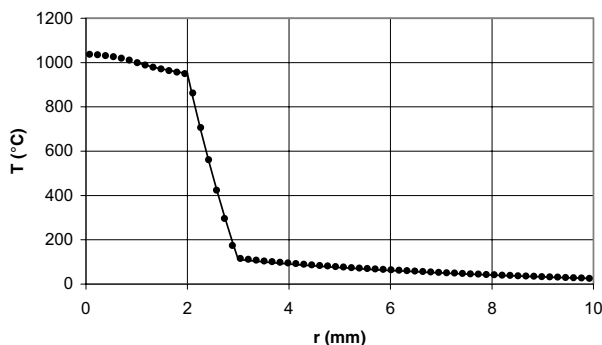


FIGURE 3. Temperature profiles for a 1 mm-radius graphite rod surrounded by concentric cylindrical shells of 1 mm of MgO , 1 mm of ZrO_2 , and 5 mm of MgO , with the surface of the graphite held at $1000 \text{ }^\circ\text{C}$. The outer boundary temperature of the outer cylinder was held at $25 \text{ }^\circ\text{C}$. The black dots show the numerical solution for grid size $n = 64$; the solid line shows the analytical solution for $r > 1 \text{ mm}$.

TABLE 2A. Current and power per 10 mm segment required to reach 1000 ± 0.1 °C at the surface of a 1 mm radius graphite rod surrounded by concentric cylinders of 1 mm thickness of MgO, 1 mm of zirconia, and 5 mm of MgO

| n | $T(r=1)$ (°C) | $T(r=2)$ (°C) | $T(r=3)$ (°C) | Power (Watts) | Current (Amps) | rms error (°C) |
|------------|---------------|---------------|---------------|---------------|----------------|----------------|
| 8 | 1000 | 706 | 536 | 1470.5 | 173.3 | 213.4 |
| 16 | 1000 | 777 | 211 | 204.11 | 44.18 | 20.8 |
| 32 | 1000 | 838 | 170 | 204.05 | 58.89 | 21.1 |
| 64 | 1000 | 924 | 133 | 262.28 | 66.77 | 4.4 |
| 128 | 1000 | 945 | 169 | 262.13 | 61.67 | 4.7 |
| 256 | 1000 | 938 | 119 | 245.27 | 59.60 | 1.20 |
| 512 | 1000 | 942 | 116 | 245.14 | 60.75 | 1.18 |
| Analytical | 1000 | 950.4 | 111.2 | 248.4 | 61.11 | 0.0 |

Notes: Temperatures are shown at $r=1$, $r=2$, and $r=3$ mm. The outer boundary temperature of the outer cylinder was held at 25 °C.

TABLE 2B. Similar to Table 2a, but in this case, the power was constrained to be constant by adjusting the heat sources to match the theoretical power value of 248.4 Watts per centimeter, while the temperature field was not constrained at any point

| n | $T(r=1)$ (°C) | $T(r=2)$ (°C) | $T(r=3)$ (°C) | Current (Amps) | rms error (°C) |
|------------|---------------|---------------|---------------|----------------|----------------|
| 8 | 140 | 111 | 90 | 48.73 | 297 |
| 16 | 645 | 501 | 143 | 48.73 | 118 |
| 32 | 642 | 539 | 116 | 64.97 | 136 |
| 64 | 948 | 876 | 127 | 64.97 | 18.2 |
| 128 | 947 | 895 | 114 | 59.97 | 17.7 |
| 256 | 1012 | 950 | 120 | 59.97 | 4.4 |
| 512 | 1013 | 955 | 117 | 61.15 | 4.4 |
| Analytical | 1000 | 950.4 | 111.2 | 61.11 | 0.0 |

the first stage anvil region and module) heats up to a variable degree during each experiment depending on the total power output, it is thought that the inclusion of the press environment not only improves the numerical behavior, but also resembles the real situation during a high-pressure experiment. Thus, the correction for the press environment was used in all the calculations presented here, and each result for completeness includes the boundary temperature T_1 of the numerical grid calculated according to Equation 7.

Example calculations

We simulated several multi-anvil assembly designs to demonstrate the use of our model and to test the correspondence between model results and experiments. To facilitate comparison, all calculations were made using a thermocouple temperature of 1200 °C. This is a temperature range of broad geological interest, but not high enough to require large extrapolations of the thermal conductivity equations for most of the materials. The calculations were all made with a grid density of 128 for the shortest axis (128 by 128 for the square cases). The thermal gradients in the sample area are depicted (Table 4) by showing three numbers: the temperature at the thermocouple, the temperature at the center of the sample, which is a saddle point in the temperature field, and the temperature at the center of the outer edge of the sample, nearest the furnace, which is the hottest point in the sample. The axial and radial temperature differences and the total temperature variation within the sample can be obtained from these numbers. Also shown is the temperature gradient at the thermocouple, in degrees per millimeter.

The different multi-anvil designs we present here are assemblies previously used at the high-pressure laboratories of SUNY Stony Brook and Arizona State University (the 14/8 “G2” assembly, Gwanmesia et al. 1990), the Bayerisches Geoinstitut (the 14/8 “Bayreuth” assembly; Poe, pers. comm.), and the Geophysical Laboratory (the 8/3 “Fei” assembly, Bertka and Fei 1997; Fei, pers. comm.). The “G2” employs a box-shaped or telescoping graphite furnace, a construction that is meant to allow a larger sample volume than straight furnaces and is used

TABLE 3. Effect of moving the boundary of the numerical grid, with and without including the press effect

| Boundary distance (mm) | T_{tc} | T_{mid} | T_{high} | ΔT | T_1 | Power | Current |
|--|----------|-----------|------------|------------|-------|-------|---------|
| Including the press: | | | | | | | |
| 6 | 1200 | 1269 | 1299 | 99 | 166 | 647 | 205 |
| 12 | 1200 | 1267 | 1297 | 97 | 93 | 669 | 208 |
| With isothermal boundary (25 °C) at boundary distance: | | | | | | | |
| 6 | 1200 | 1279 | 1314 | 114 | 25 | 790 | 226 |
| 12 | 1200 | 1271 | 1303 | 103 | 25 | 734 | 218 |

Notes: Constant grid density of 0.1875 mm, 14/8 assembly “G2.” T_{tc} is the temperature at the thermocouple; T_{mid} at the sample center, and T_{high} at the hottest point along the outer central perimeter of the sample, ΔT is the total gradient in the sample, and T_1 is the temperature at the outer boundary of the numerical grid.

TABLE 4. Summary of cell assemblies and temperature gradients calculated for a thermocouple temperature of 1200 °C, and radial grid size of 128

| Cell | Power (W) | T_{tc} (°C) | T_{mid} (°C) | T_{high} (°C) | $(dT/dz)_{tc}$ (°C/mm) | T_{anvil} (°C) | r_{max} (mm) | T_1 |
|-----------------------------------|-----------|---------------|----------------|-----------------|------------------------|------------------|----------------|-------|
| Watson 19 mm piston-cylinder | 2396 | 1200 | 1215 | 1218 | 8 | 309 | 15 | 168 |
| 14/8 “G2” | 648 | 1200 | 1248 | 1274 | 87 | 310 | 8 | 117 |
| 14/8 Bayreuth: LaCrO ₃ | 390 | 1200 | 1222 | 1224 | 89 | 174 | 8 | 87 |
| 14/8 Bayreuth: graphite | 574 | 1200 | 1230 | 1233 | 102 | 294 | 8 | 117 |
| 8/3 Fei | 202 | 1200 | 1236 | 1249 | 112 | 242 | 5 | 78 |

Notes: T_{tc} is the temperature at the thermocouple, T_{mid} is at the saddle point at the assembly center, and T_{high} is at the hottest point in the sample. T_{anvil} is the maximum temperature experienced by the tungsten carbide anvils, and T_1 is the temperature at the boundary of the numerical grid. The outside of the press was held at 25 °C in every case.

for hot-pressing or sample synthesis. The Bayreuth assembly implements both a stepped LaCrO₃ or graphite heater, and a zirconia ceramic insulating sleeve outside the furnace. The Fei assembly uses a metal foil heater with LaCrO₃ thermal insulation. However, we started with a piston-cylinder design (Watson et al. 2002) because its thermal gradient is well characterized and acts as a good test of the performance of the model in a real case.

Watson assembly. The Watson et al. (2002) piston-cylinder assembly employs a straight graphite heater with a graphite

pickup cap on one end. For thermal insulation, concentric sleeves of pyrex (inner sleeve) and NaCl (outer sleeve) surround the outside of the furnace, and the NaCl allows ductile flow of the assembly under pressure. The assembly is enclosed in a tungsten-carbide cylinder, is bounded at one end by a tungsten-carbide piston, and at the other end by a stainless steel base-plug. In our calculation, we filled the furnace with concentric alumina and MgO sleeves, to match the arrangement used to measure the temperature estimated by Watson et al. (2002), in which the profile along the MgO-Al₂O₃ boundary was measured by looking at the thickness of the reaction layer of MgAl₂O₄. This assembly is asymmetric, so the full assembly was calculated without a central mirror plane. Also, the assembly is highly elongated, so the calculation used an aspect ratio of 4. The grid size was $r_{\max} = 128$, $z_{\max} = 512$.

The resulting thermal profile for 1200 °C is shown in Figure 4a, which shows the model for positive r and all z (or the $+r$ half of the total cross-section of the assembly). MgO and alumina have similar thermal conductivities at high temperature (Figs. 2a and b) so the sleeves used for the thermal gradient measurement caused little local perturbation in the temperature contours. Because the furnace is elongated, the hot zone of the furnace has a significant useful length, of over 7 mm, from the point where the thermocouple is located (shown as a small circle on the diagram; the thermocouple wire itself is not explicitly modeled in any of the current calculations) to the 1200 °C contour on the opposite side. For the sample region located in this area with a length of 7.6 mm and a diameter of 5 mm, the total thermal gradient is 18 °C.

The thermal gradient measurement in Watson et al. (2002) was made at a thermocouple temperature of 1400 °C, with the thermocouple located at the saddle point in temperature, so we also performed a calculation under that condition to test the similarity of the model to the measurement. Our axial thermal gradient is very similar to theirs, with the region over 1200 °C occupying about 50% of the total length of the furnace, and the contours in similar locations. The 1200 °C contours are 19 mm apart in the measurements by Watson et al. (2002) and 22.5 mm apart in our calculation (our dimensions were not corrected for compression). The radial gradient in the model is somewhat less than in the measurement; the measured radial gradient is over 20 °C from the center to a radius of 4 mm, while ours is 10 °C over the same distance, and there is no 1420 °C contour in our model. Despite the differences, the overall agreement is reasonable. Knowledge of the thermal conductivity of pyrex under the conditions of the experiment could be helpful in improving this agreement; it is notable that the conditions are well beyond the available thermal conductivity measurements for pyrex. It appears that the real thermal conductivity of pyrex under these conditions may be lower than in our model.

“G2” 14/8 assembly. The first multi-anvil design tested was the “G2” assembly (Gwanmesia et al. 1990; Leinenweber and Parise 1994). This assembly is a typical “box furnace” design, used to produce large samples. The graphite furnace surrounds the sample, providing heat from the ends of the sample as well as from around its circumference. The electric current is brought to the furnace through molybdenum leads, and the furnace is insulated with zirconia ceramic. The sample area is surrounded

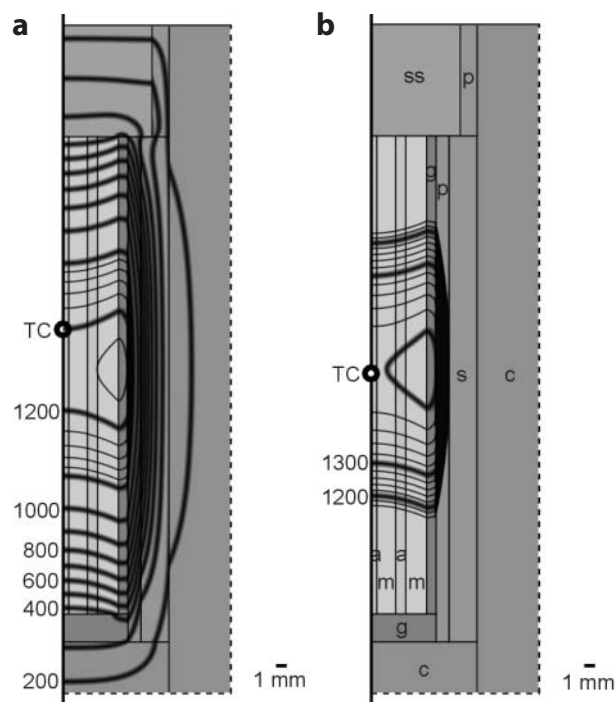


FIGURE 4. Thermal profiles calculated for the Watson 19 mm piston-cylinder assembly. The physical size of the model was 15 mm by 60 mm, and the model had an aspect ratio (z_{\max}/r_{\max}) of 4, with a grid density of 128×512 . The r -axis is to the right and the z -axis is down in this and the other assembly pictures (Figs. 4-7). The dotted boundaries are isothermal boundaries, while the solid boundary is the zero-flux boundary at $r = 0$. The thermocouple is shown as a circle on each diagram. (a) The full thermal profile calculated for a thermocouple temperature of 1200 °C. The major contour interval is 100 °C; minor contours are shown at 20 °C intervals from 1100 °C up. The boundary temperature is 168 °C. (b) Temperatures calculated with the thermocouple near the saddle point and at a temperature of 1398 °C. The thicker contours are the 1200, 1300, and 1400 °C contours; contours are shown at a 20 °C interval from 1160 °C up. The boundary temperature is 193 °C. This picture is drawn with the same contours and is intended for direct comparison to Figure 10 of Watson et al. (2002). Materials are (a) Al₂O₃, (m) MgO, (g) C (graphite) (dark gray), (p) pyrex, (s) salt (NaCl), (ss) stainless steel, and (c) carbide (WC).

by MgO sleeves, and a platinum capsule and MgO sample are used. The capsule is 3.5 mm in outer diameter and 3.2 mm in length. Unlike the piston-cylinder assembly of Watson et al. (2002), this assembly can be approximated as being symmetrical about the central plane; this plane was chosen as the $z = 0$ plane, and the rest of the assembly was generated by a mirror across this plane (top edge of the drawing) as well as by the required revolution about the $r = 0$ line (left edge of the drawing). The mirror plane and central line were both modeled as zero-flux boundaries, as described in the experimental section, while the other two boundaries acted as heat sinks. The model calculated the heat production of the furnace using a radial current flow in the graphite caps, with a $1/r$ dependence of current density, and a constant current density in the cylindrical part of the furnace. The thermal profile calculated for this assembly is shown in Figure

5. Only the explicitly modeled region (the $+r$, $+z$ quadrant of the assembly) is shown in the Figure.

This assembly has a total calculated temperature difference of 74 °C across the sample at 1200 °C. Although in designing the assembly, MgO was chosen as a thermal distributor around the sample based on the fact that its thermal conductivity at room temperature is thirty times higher than that of ZrO₂, the actual difference at the experimental conditions was only a factor of two (Fig. 2). This reduces the effectiveness of MgO as a thermal distributor, so the gradient in the sample is somewhat larger than it would be if the room-temperature thermal conductivities were still obeyed; in the hypothetical case where all the components retain their room-temperature thermal conductivities, a temperature difference of 52 °C across the sample would be attained at a thermocouple temperature of 1200 °C. ZrO₂ still acts as an effective thermal barrier because of its overall low conductivity, which is similar throughout the temperature region from ambient temperature to 1200 °C. The primary cause of the gradient is the thick molybdenum current ring, which is used to carry the high current required for the graphite furnace, but also acts as a “coldfinger” into the sample area.

Bayreuth 14/8 assembly. The Bayreuth 14/8 assembly (B. Poe, pers. comm.) uses either lanthanum chromite or graphite as a furnace, and zirconia as an insulator. It also has molybdenum pickup rings, but much shorter ones only at the furnace ends, and the furnace is an axial “step-heater” with a thicker central portion and thinner ends. The step-heater acts somewhat like a 3-zone furnace, in that the end zones produce more heat and the central zone less, but unlike in a 3-zone furnace, the relative heat production at each zone is fixed in advance by the dimensions of the assembly and cannot be varied during the run. The heat production of each segment of the furnace was built in to the model by making the current density inversely proportional to the cross-sectional area of the furnace, as usual. The thermal distributions calculated for this assembly are shown in Figure 6.

The temperature difference in the sample/capsule area (1.6 mm in diameter and 2.4 mm in length) calculated for a lanthanum chromite furnace is 24 °C and for a graphite furnace is 33 °C. Although the full temperature distribution varies between the two furnaces, as seen in the figure, due to the differing thermal conductivities and the temperature dependence of their electrical conductivities, the differences in the gradients within the sample are small. The most significant differences are in the furnace itself; the lanthanum chromite furnace supports higher thermal gradients, due to its low thermal conductivity, and also heats more at the ends than at the center because of its higher resistance at low temperature.

The graphite furnace, because of its high thermal conductivity, has the disadvantage of transferring more heat into the surroundings, so the power consumption is about 50% higher, and the anvil temperature is also much higher (Table 4). Ultimately, the choice between lanthanum chromite and graphite is made for reasons such as avoiding chromium contamination (graphite), or avoiding the transition of the furnace to diamond (lanthanum chromite). We conclude that for this particular assembly, the choice can be made without much concern for its effects on the thermal gradients within the sample.

Fei 8/3 assembly. The 8/3 “Fei” assembly (Bertka and Fei

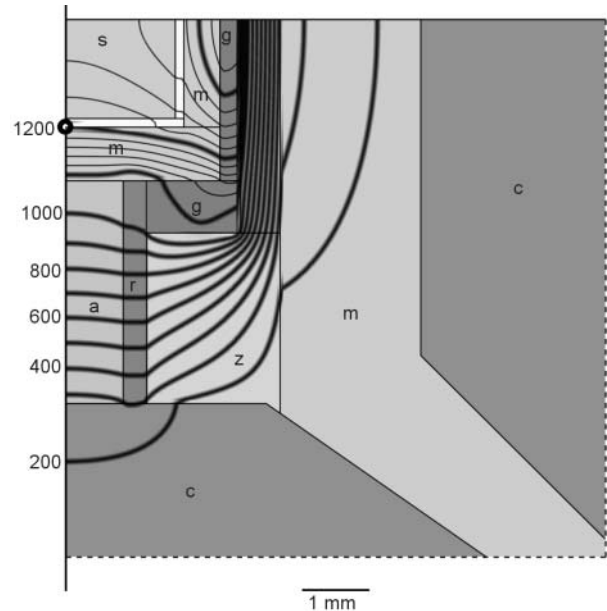


FIGURE 5. Contour diagram of the calculated temperature field for the 14/8 “G2” assembly. The diagram uses the same contour intervals as Figure 4a. The boundary temperature was 117 °C. The grid size for this and the next 3 assemblies (Figs. 4-7) was 128 by 128. Materials from the center out are: s = MgO sample, platinum capsule (light color), m = MgO sleeve, a = Al₂O₃ rod; r = Mo ring; g = C (graphite) furnace (dark color), z = ZrO₂ insulation, m = MgO octahedron, and c = WC anvils. The physical size of the model is 8 mm by 8 mm.

1997) is an example of an assembly that uses a small metal foil furnace. The furnace is made of platinum foil surrounded by LaCrO₃, which in this case acts as a thermal barrier and not as an active heating element (note that the standard experimental assembly uses rhenium foil, but platinum was used in the calculation). The inside of the assembly consists of alumina caps, an MgO central sleeve, and MgO sample with a length of 1.4 mm and a diameter of 1 mm (in our model). The thermocouple is axial, placed at the cool end of the sample, 0.7 mm from the sample center.

The calculated temperature difference in the sample region is 49 °C. This temperature difference is mainly due to the conduction out the ends of the assembly, since the thick LaCrO₃ sleeve in the radial direction is highly insulating. In the real case, the thermocouple side has some zirconia cement, so that side might be more insulating and the actual gradient asymmetric. Another source of asymmetry would be greater heating from the thermocouple side, where slits are cut in the furnace to allow the thermocouple to pass through.

The calculated gradient may be compared in a general sense to the experimental gradient derived from spinel growth kinetics by van Westrenen et al. (2003) using the same assembly. Their experiment L-238 was performed at 1700 °C. Their total axial gradients, read from their Figure 7 assuming that the data represents a smooth, convex downward axial gradient similar to our calculations, are 50 °C in 0.5 mm and 150 °C in 1 mm. The calculated values at 1200 °C are 40 and 98 °C. We did

not perform a more direct comparison, in lieu of a good model for extrapolating the thermal conductivity of LaCrO_3 to higher temperatures. However, direct scaling of the result from 1200 to 1700 °C gives values of 68 and 140 °C, which are reasonably close to the experimental values.

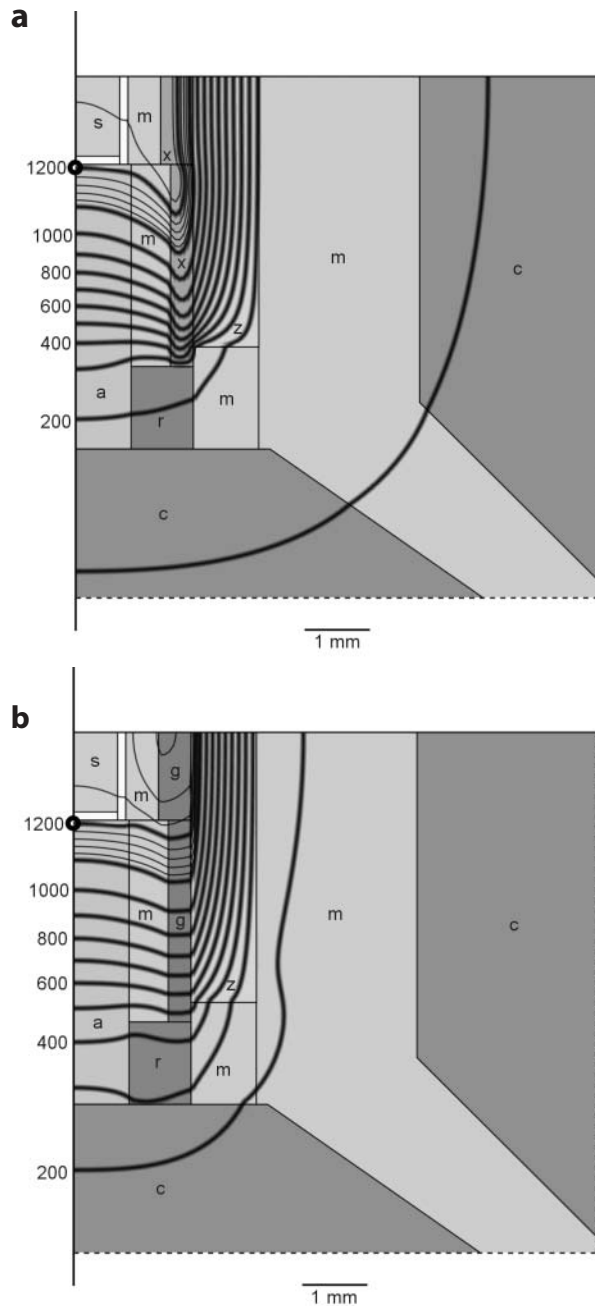


FIGURE 6. Calculated thermal gradient for Bayreuth heater (a) With a lanthanum chromite furnace, and (b) with a graphite furnace. The diagram uses the same contour intervals as Figure 4a. The boundary temperatures are 87 °C (Fig. 6a) and 117 °C (Fig. 6b). The physical size of the model is 8 mm by 8 mm. Materials are s = MgO sample; Pt capsule (lighter color); a = Al_2O_3 rod; r = Mo ring; m = MgO sleeves; x = LaCrO_3 furnace or g = C (graphite) furnace; z = ZrO_2 sleeve, m = MgO octahedron, c = WC anvils.

Conclusions. Several conclusions can be made from these sample calculations. First, despite the differences in the assemblies calculated, the overall temperature distributions are similar in form. The magnitudes of the gradients that were deemed acceptable by the designers of the assemblies are reflected in the size of the sample region that is utilized in each assembly and the temperature difference across that region. At a thermocouple temperature of 1200 °C, the total gradient in the sample ranges from 24 °C (the Bayreuth 14/8 assembly with a lanthanum chromite furnace) to 74 °C (the “G2” assembly), but with a variety of sample sizes and pressure/temperature capabilities, depending on the assembly.

One feature that all the multi-anvil assemblies studied here have in common is that the thermocouple is placed at a location of high thermal gradient, on the order of 100 °C/mm near the cold end of the sample. All of the useful volume is taken up by the sample, and the thermocouple is placed at the edge of the useful volume, where the strong gradients begin. Also, when metal capsules are used as in several of these calculations, the thermocouple is in a thermal boundary layer, a region of enhanced gradients, next to the thermally conducting capsule. This means that small differences in positioning of the thermocouple can cause significant differences in the measured temperatures. For these reasons, care needs to be taken in designing experiments to ensure the placement of thermocouples at reproducible locations. Also, the value of the thermal gradient in the region of the thermocouple, in addition to the thermal gradient in the sample itself, needs to be considered in the future design of better assemblies.

These examples serve to show the utility of this model for analyzing thermal distributions in multi-anvil assemblies and learning more about the assemblies from the analysis. The

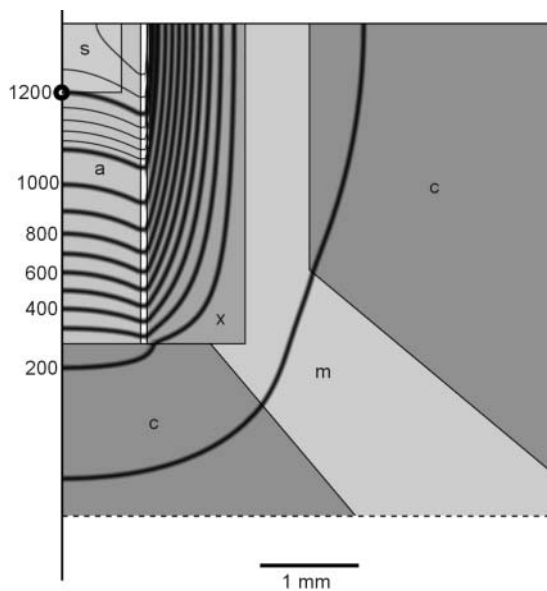


FIGURE 7. Thermal calculation for the 8/3 larger “Fei” assembly. The diagram uses the same contour intervals as Figure 4a. The boundary temperature is 78 °C. The physical size of the model is 5 mm by 5 mm. Materials are s = MgO “sample;” a = Al_2O_3 rod; Pt furnace (lighter color); x = LaCrO_3 sleeve; m = MgO octahedron, and c = WC anvils.

range of assemblies in actual use is very wide and continuously evolving, and a full analysis of the effects of design parameters on thermal gradients is a continuing project that will require the use of numerical procedures such as the ones outlined here. It is hoped that by coupling this analysis with the design and testing of real assemblies, the thermal gradients in multi-anvil assemblies can be greatly reduced, or the sample volumes for a given thermal gradient increased.

ACKNOWLEDGMENTS

This project was initiated as a senior thesis project at Arizona State University by JH. This research was partially supported by COMPRES, the Consortium for Materials Property Research in Earth Sciences under NSF cooperative agreement EAR 01-35554. It was also partially supported by grant NSF EAR 0073987 to JAT.

REFERENCES CITED

- Bertka, C.M. and Fei, Y. (1997) Mineralogy of the Martian interior up to core-mantle boundary pressures. *Journal of Geophysical Research*, 102, 5251–5264.
- Brandt, A. (1977) Multilevel adaptive solutions to boundary-value problems. *Mathematics of Computation*, 31, 333–390.
- Carslaw, H.S. and Jaeger, J.C. (1959) *Conduction of Heat in Solids*. Oxford University Press.
- Fujisawa, H., Fujii, N., Mizutani, H., Kanamori, H., and Akimoto, S.I. (1968) Thermal diffusivity of Mg_2SiO_4 , Fe_2SiO_4 and NaCl at high pressures and temperatures. *Journal of Geophysical Research*, 73, 4727–4733.
- Funamori, N. and Yagi, T. (1993) High-pressure and high-temperature in-situ X-ray observation of $MgSiO_3$ perovskite under lower mantle conditions. *Geophysical Research Letters*, 20, 387–390.
- Gwanmesia, G.D., Liebermann, R.D., and Guyot, F. (1990) Hot-pressing and characterization of polycrystals of β - Mg_2SiO_4 for acoustic velocity measurements. *Geophysical Research Letters*, 17, 1331–1334.
- Hampel, C. (1961) *Rare Metals Handbook*, p. 715. Reinhold Pub. Corp., New York.
- Hofmeister, A.M. (1999) Mantle values of thermal conductivity and the geotherm from phonon lifetimes. *Science*, 283, 1699–1706.
- Katsura, T. (1997) Thermal diffusivity of periclase at high temperatures and high pressures. *Physics of the Earth and Planetary Interiors*, 101, 73–77.
- Kawai, N. and Endo, S. (1970) The generation of ultrahigh hydrostatic pressures by a split sphere apparatus. *Review of Scientific Instruments*, 41, 1178–1181.
- Kingery, W.D. (1959) Thermal Conductivity. 14. Conductivity of Multicomponent Systems. *Journal of the American Ceramic Society*, 42, 617–627.
- Kingery, W.D., Francl, J., Coble, R.L., and Vasilos, T. (1954) Thermal Conductivity: X, Data for Several Pure Oxide Materials Corrected to Zero Porosity. *Journal of the American Ceramic Society*, 37, 107–110.
- Laubitz, M.J. and Venderme, M.P. (1966) Thermal conductivity of platinum between 300 and 1000 degrees K. *Canadian Journal of Physics*, 44, 3173–3184.
- Leinenweber, K. and Parise, J.B. (1994) High pressure synthesis and crystal structure of $CaFeTi_2O_6$, a new perovskite structure type. *Journal of Solid State Chemistry*, 114, 277–281.
- McQuarrie, M. (1954) Thermal conductivity: VII, Analysis of variation of conductivity with temperature for Al_2O_3 , BeO, and MgO. *American Ceramic Society Bulletin*, 37, 91–95.
- Oran, E.S. and Boris, J.P. (1987) *Numerical Simulation of Reactive Flow*. Elsevier, New York.
- Ringwood, A.E. and Major, A. (1966) Synthesis of Mg_2SiO_4 - Fe_2SiO_4 spinel solid solutions. *Earth and Planetary Science Letters*, 1, 241–245.
- Sakai, N. and Stolen, S. (1995) Heat capacity and thermodynamic properties of lanthanum(III) chromate(III): $LaCrO_3$, at temperatures from 298.15 K, Evaluation of the thermal conductivity. *Journal of Chemical Thermodynamics*, 27, 493–506.
- Schilling, F. and Wunder, B. (2004) Temperature distribution in piston-cylinder assemblies: Numerical simulations and laboratory experiments. *European Journal of Mineralogy*, 16, 7–14.
- Schmidt, M.W. and Ulmer, P. (2004) A rocking multi-anvil: Elimination of chemical segregation in fluid-saturated high-pressure experiments. *Geochimica et Cosmochimica Acta*, 68, 1889–1899.
- Taylor, R., Gilchris, Ke, and Poston, L.J. (1968) Thermal conductivity of polycrystalline graphite. *Carbon*, 6, 537–544.
- van Westrenen, W., Van Orman, J.A., Watson, H., Fei, Y., and Watson, E.B. (2003) Assessment of temperature gradients in multi-anvil assemblies using spinel layer growth kinetics. *Geochemistry, Geophysics, Geosystems*, 4, doi: 10.1029/2002GC000474.
- Walker, D., Carpenter, M.A., and Hitch, C.M. (1990) Some simplifications to multi-anvil devices for high pressure experiments. *American Mineralogist*, 75, 1020–1028.
- Walter, M.J., Thibault, Y., Wei, K., and Luth, R.W. (1995) Characterizing experimental pressure and temperature conditions in multi-anvil apparatus. *Canadian Journal of Physics*, 73, 273–286.
- Watson, E.B., Wark, D.A., Price, J.D., and Van Orman, J.A. (2002) Mapping the thermal structure of solid-media pressure assemblies. *Contributions to Mineralogy and Petrology*, 142, 640–652.
- Yamazaki, D. and Karato, S.-I. (2001) High-pressure rotational deformation apparatus to 15 GPa. *Review of Scientific Instruments*, 72, 4207–4211.

MANUSCRIPT RECEIVED MARCH 10, 2005

MANUSCRIPT ACCEPTED JUNE 1, 2005

MANUSCRIPT HANDLED BY ALISON PAWLEY